

Self-consistent formation and steady-state characterization of trapped high-energy electron clouds in the presence of a neutral gas background

Cite as: Phys. Plasmas **29**, 082105 (2022); <https://doi.org/10.1063/5.0098567>

Submitted: 10 May 2022 • Accepted: 10 July 2022 • Published Online: 05 August 2022

 G. Le Bars,  J.-Ph. Hogge,  J. Loizu, et al.



View Online



Export Citation



CrossMark

ARTICLES YOU MAY BE INTERESTED IN

Mode conversion from kinetic Alfvén waves to modified electron acoustic waves
Physics of Plasmas **29**, 082104 (2022); <https://doi.org/10.1063/5.0093193>

Observation and analysis of a large banana orbit in the diocotron mode of a coaxial Malmberg-Penning trap

Physics of Plasmas **29**, 082103 (2022); <https://doi.org/10.1063/5.0098959>

Electron heating in 2D: Combining Fermi-Ulam acceleration and magnetic-moment non-adiabaticity in a mirror-configuration plasma

Physics of Plasmas **29**, 082106 (2022); <https://doi.org/10.1063/5.0097299>



Self-consistent formation and steady-state characterization of trapped high-energy electron clouds in the presence of a neutral gas background

Cite as: Phys. Plasmas **29**, 082105 (2022); doi:10.1063/5.0098567

Submitted: 10 May 2022 · Accepted: 10 July 2022 ·

Published Online: 5 August 2022



View Online



Export Citation



CrossMark

G. Le Bars,^{1,a)} J.-Ph. Hogge,¹ J. Loizu,¹ S. Alberti,¹ F. Romano,¹ and A. Cerfon²

AFFILIATIONS

¹Ecole Polytechnique Fédérale de Lausanne (EPFL), Swiss Plasma Center (SPC), CH-1015 Lausanne, Switzerland

²Courant Institute of Mathematical Sciences, New York University, New York, New York 10012, USA

^{a)}Author to whom correspondence should be addressed: guillaume.lebars@epfl.ch

ABSTRACT

This study considers the self-consistent formation and dynamics of electron clouds interacting with a background neutral gas through elastic and inelastic (ionization) collisions in coaxial geometries similar to gyrotron electron guns. These clouds remain axially trapped as the result of crossed magnetic field lines and electric equipotential lines creating potential wells similar to those used in Penning traps. Contrary to standard Penning traps, in this study, we consider a strong externally applied radial electric field which is of the same order as that of the space-charge field. In particular, the combination of coaxial geometry, strong radial electric fields, and electron collisions with the residual neutral gas (RNG) present in the chamber induce non-negligible radial particle transport and ionization. In this paper, the dynamics of the cloud density and currents resulting from electron–neutral collisions are studied using a 2D3V particle-in-cell code. Simulation results and parametric scans are hereby presented. Finally, a fluid model is derived to explain and predict the cloud peak density and peak radial current depending on the externally applied electric and magnetic fields, and on the RNG pressure.

© 2022 Author(s). All article content, except where otherwise noted, is licensed under a Creative Commons Attribution (CC BY) license (<http://creativecommons.org/licenses/by/4.0/>). <https://doi.org/10.1063/5.0098567>

I. INTRODUCTION

Non-neutral plasmas are relevant to many fields in physics and engineering, for example, elementary particle physics,¹ particle accelerators,² or high-power microwave sources such as gyrotrons.³ They present confinement properties and types of instabilities that make them fundamentally different from quasi-neutral plasmas.² Non-neutral plasmas have been studied since the 1960s in various configurations, the most common being the Penning–Malmberg trap: a cloud of single-sign-charged particles is trapped in a cylindrical chamber by a strong axial magnetic field and two end electrodes imposing a confining axial electric field.⁴ This configuration is predominantly used to study the behavior of elementary particles at low and extremely low temperatures.⁴

In Penning–Malmberg traps, the equilibrium and dynamics of charged particle clouds (electrons or ions) are dominated by long-range collective effects associated with the electric field self-generated by the plasma. The total trapped charge is controlled externally through the axial magnetic field, the end electrodes voltage, and the

external particle source.¹ The level of vacuum inside the device is such that ionization processes between the confined charges and the background neutrals can be neglected. To ensure that the equilibrium state exists over very long time scales,⁵ many dedicated theoretical and experimental studies have been carried out to avoid disruptive instabilities such as the azimuthal diocotron instability^{6–16} and, to a lesser extent, axial resonant space-charge effects.¹ The confining electric potential along the magnetic field lines, which is imposed externally, is generally of the order of tens of V and the trapped plasma densities are low with a Brillouin ratio $2\omega_{pe}^2/\Omega_{ce}^2 \ll 1$, where ω_{pe} is the plasma frequency and Ω_{ce} is the electron cyclotron frequency.¹ The cloud temperature is initially determined by the mechanisms of electron generation and injection, and the cloud is often further cooled to temperatures of the order of a few eV to reduce the electron neutral collision cross sections and increase the confinement time, or cooled to extremely low temperatures (a few K) to study quantum effects.¹ The cloud dynamics is characterized by a net rotation velocity that is generally non-relativistic and is given by the $\vec{E} \times \vec{B}$ drift, with the radial component of the electric field, E_r , determined by the cloud

space-charge. This rotational velocity provides an inward-pointing $\vec{v} \times \vec{B}$ force that balances the radially outward electric force.

The study of non-neutral plasmas is also relevant to the development of gyrotron electron guns, where secondary electron clouds (i.e., not belonging to the main electron beam) can remain locally trapped and accumulate in effective potential wells due to the local electric and magnetic field topology.^{17,18} The trapped electrons, if released by instabilities or shielding of the wells by space-charge effects, can lead to detrimental and even damaging currents that prevent nominal gyrotron operation. These potential well traps are very similar to the ones used in Penning–Malmberg traps. However, in the case of the gyrotron gun, the magnetic field is non-uniform and the electric field has a strong, externally imposed, radial component, with only a fraction of the total electric field given by the trapped electron cloud space-charge itself. Due to the resulting strong azimuthal $\vec{E} \times \vec{B}$ drift, the trapped electrons have sufficient kinetic energy to ionize the residual neutral gas (RNG) in the gyrotron vacuum chamber. Such ionization phenomena, combined with the existence of trapping potential wells, have been linked to the observed detrimental currents in gyrotron guns.¹⁸ To avoid this problem, a design criterion has been defined which imposes the absence of any vacuum potential well in the electron gun by a careful modification of the shapes of the electrodes.¹⁷ However, this process becomes highly demanding from an engineering point of view, and relaxed design criteria are highly desirable. This work is particularly relevant to the research effort in magnetically confined fusion plasmas, as gyrotrons are foreseen to play a major role in heating, current drive, and instability control of fusion plasmas¹⁹ in tokamaks, such as ITER,²⁰ the Divertor Tokamak Test facility (DTT),²¹ or the DEMOnstration power plant,²² and in stellarators such as Wendelstein 7-X.²³

At the time of writing, there has been no study, to the authors' knowledge, of electron trapping in chambers with azimuthal symmetry that are subject to strong external radial electric fields, and in which electron–neutral collisions dominate the sources and sinks of electrons. Collisions between trapped particles and RNG in the vacuum chamber lead to radial transport. Such phenomena have been studied using a kinetic model²⁴ or a fluid model^{25,26} but without considering ionization as a source of electrons. Studies including ionization effects have been done using a fluid model considering cold²⁷ or hot isothermal plasmas²⁸ but neglecting inertial effects. Furthermore, none of these studies considered non-uniform magnetic fields or external radial electric fields.

This study presents fully kinetic numerical simulations that simultaneously take into account electron–neutral elastic and inelastic (ionization) collisions, strong externally imposed electric fields, as well as axial and radial non-uniformities typical of gyrotron guns (geometry, magnetic field, external electric field). To explain the simulation results, an analytical fluid model is derived that highlights the parametric dependence of peak density and leaking currents associated with the formation of electron clouds.

A 2D3V particle-in-cell (PIC) code, assuming azimuthal symmetry, has been developed and used to characterize the self-consistent electron cloud formation in a gyrotron electron gun due to RNG ionization. Contrary to the traditional Penning–Malmberg trap, the geometry of interest has a coaxial configuration, and the trapped electron cloud presents a hollow density profile. This is a significant difference compared to the filled cylindrical column stored in Penning–Malmberg traps, as it has been shown that annular non-neutral plasma clouds are

highly susceptible to the diocotron instability.^{2,14} However, this instability is not considered in the present study.

The article is divided into the following sections: Sec. II describes the numerical method and the geometry of interest, while Sec. III presents the main findings from individual PIC simulations, specifically the type of losses, the dominant forces in each direction, and shows the results of parametric scans highlighting the dependencies of the cloud peak density and current on the key parameters of the system. To explain these dependencies, a fluid–Poisson model is derived and compared to the numerical results in Sec. IV. A summary of the simulation results and density and current dependencies on external parameters and related discussions makeup the last section of the paper, Sec. V.

II. METHODS

A. Numerical model

An electrostatic 2D3V, PIC code has been developed that solves the collisional Vlasov–Poisson equation for the electron distribution function $f_e(\vec{r}, \vec{v}, t)$ and the electric potential $\phi(\vec{r}, t)$. This code uses a cylindrical coordinate system (r, θ, z) and assumes azimuthal symmetry ($\partial_\theta = 0$). The Poisson equation is solved using a finite element method (FEM) based on weighted extended b-splines of any order.^{29,30} This method allows the definition of Dirichlet boundary conditions on curved surfaces while keeping a rectangular grid for the finite element method and allowing flexibility in the choice of geometries. With such a numerical method, the non-trivial geometry of the electron gun can be easily approximated in the code without needing an optimized, often complex, mesh adapted to the particular geometry, as with traditional finite element methods based on triangular cells. Indeed, this technique improves the flexibility and rapidity to explore different geometries. The use of a rectangular grid also simplifies the parallelization of the code using both multiple nodes (MPI) and multiple cores in each node (openMP). The Vlasov equation is solved for f_e using the standard PIC method by sampling this distribution function with macro-particles and by calculating the trajectory of each macro-particle using the Boris algorithm.³¹ The particle boundary conditions are perfectly absorbing, and the electric potential boundary conditions are a mix of Dirichlet on the metallic parts, and Neumann on the open boundaries. This is illustrated in Fig. 1, where the gray parts, representing metallic boundaries, are set at a fixed potential, while Neumann

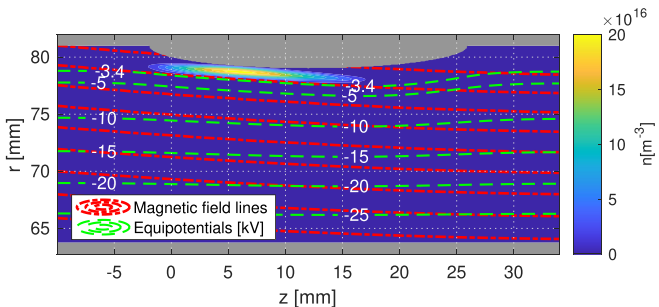


FIG. 1. Geometry and simulation domain. The top and bottom gray parts represent the metallic boundary conditions with an externally imposed bias of $\Delta\phi = 30$ kV. The peak magnetic field amplitude in this domain, here in the lower right corner, is $B_{\max} = 0.28$ T. The cloud density and self-consistent electric equipotential lines are represented at a time when the number of trapped electrons is maximum.

boundary conditions are imposed at $z_L = -10$ mm and $z_R = 34$ mm in the blue region, $\partial_z \phi(z = z_L) = \partial_z \phi(z = z_R) = 0$.

To initiate the cyclic self-consistent cloud formation, a volumetric seed source of electrons is used as a low-intensity source spanning the full simulation space and the full simulation time. This creates electrons according to a uniform distribution function in space and a Maxwellian distribution function in velocity. This mimics the background, low-density, free-electrons present in the electron gun region due to field electron emission of the metallic surfaces or due to ionization of the RNG by natural background radiation. The source term is set such that, once a cloud is formed, the seed source is negligible compared to the ionization source.

An electron-neutral collision module has been implemented using a Monte Carlo approach.^{32,33} This module simulates elastic and ionization collisions of the electrons with the RNG in the vacuum chamber. Inelastic excitation collisions are currently not considered due to the low-excitation cross sections in the kinetic energy range of the trapped electrons and due to the high computational cost of calculating cross sections for each time step. Indeed, for the neutral gas considered in this study (Ne), at the typical electron kinetic energy of $E_k > 200$ eV, the ratio between the ionization cross section and the most probable excitation collision is $\sigma_{io}/\sigma_{1S2} > 10$ and the ratio for the next probable excitation state is $\sigma_{io}/\sigma_{2P1} > 100$.^{34,35} Similarly, for lower-energy ranges ($E_k < 200$ eV), the elastic collisions are dominating, with $\sigma_{ela}/\sigma_{1S2} > 10$.^{34,35} This module also assumes that the neutral density and temperature are constant in time and uniform and that only one type of gas is present. The nature and density of the gas are input parameters set at the beginning of the simulation. The RNG temperature is set at 300 K for the calculation of the pressure, and the neutral velocity is assumed to be zero for the calculation of the cross section. Using this approximation, the velocity of the newly formed ions is $v_{ions} \approx 0$. These ions are then subject to a fast $\vec{E} \times \vec{B}$ drift which, because of the initial conditions, imposes an ion cyclotronic velocity $v_{\perp,ions} \approx v_{E \times B}$. The ion Larmor radius is, therefore, $\rho_{L,ions} = v_{E \times B} / \Omega_{ci}$, with Ω_{ci} the ion cyclotron frequency. For electric and magnetic field amplitudes typical of gyrotron electron guns, the ion Larmor radius $\rho_{L,ions}$ is of the order of meters, which is much larger than the radial dimensions Δr of the vacuum vessel ($\rho_{L,ions}/\Delta r \gg 1$). This causes the ions created by ionization to collide with the metallic boundaries of the vacuum vessel and to be lost with a characteristic time scale $\tau_{l,ions} \approx v_{E \times B} / \Delta r \ll \tau_{io}$ much smaller than the ionization time scale τ_{io} . For realistic electron gun pressure of $p_n = 1 \times 10^{-6}$ mbar, the ion fraction $n_i/n_e \approx \tau_{l,ions}/\tau_{io} \approx 10^{-6}$ is extremely low and the ionic population would not significantly change the electric field. Furthermore, with such low levels of ion densities, the ion-resonance instability would presumably not grow although a verification of this would require simulations without azimuthal symmetry.³⁶ For these reasons, the ions formed by ionization are not simulated. Concerning elastic collisions, the cross section for momentum exchange is extracted from the LXCat library^{34,35} and re-scaled according to an analytical differential cross section to obtain the elastic scattering cross section.³⁷ The scattering angle, which is dependent on the incoming electron kinetic energy, is calculated using a random number generator and the same analytical differential cross section.³⁷ For the inelastic ionization collisions, the total ionization cross section is also extracted from the LXCat library.^{34,35} At the moment of collision, the incoming electron kinetic energy is reduced by the binding energy

of the freed electron and is distributed unevenly between the incoming and freed electron. The ratio of kinetic energy between incoming and freed electrons is calculated using an energy differential cross section based on experimental measurements.³⁸ The freed and incoming electron undergo a scattering event, and the scattering angles are calculated using the same analytical differential cross section as for elastic collisions.³⁷ In essence, the elastic collisions act as a drag term in the force balance equation for the electrons, while the ionizing collisions act as a source of electrons in the continuity equation, and as an effective drag in the force balance equation. Details on the numerical model and on the verification of its implementation will be presented in a future publication.

B. Geometry and numerical parameters

The geometry used in this study, represented in Fig. 1, is based on the electron gun geometry used in the first prototype¹⁷ of the 170 GHz 2 MW coaxial gyrotron designed for ITER, see Fig. 2. This particular Magnetron Injection Gun (MIG) was subject to voltage breakdown and detrimental leakage currents for specific magnetic field configurations and had to be redesigned to allow nominal operation.¹⁷ The configuration of this study focuses on the corona ring region of the original prototype gun and uses the same magnetic field used for the prototype gyrotron with $B \sim 0.28$ T.³⁹ This magnetic field is obtained by solving the Biot-Savart law using the actual superconducting magnet geometry and coil currents defined for the operation of this prototype gyrotron.³⁹ The field lines are slightly divergent, and the magnetic field has a mirror ratio $R = \max(B(s))/\min(B(s)) = 1.07$, where $\max(B(s))$ and $\min(B(s))$ are, respectively, the maximum and minimum amplitude of the magnetic field along a given field line. Its amplitude is a free parameter that can be modified by scaling the coil currents accordingly. The corona ring region can be approximated by a coaxial configuration as represented in Fig. 1, with a central conductor of radius $r_a = 63.75$ mm, and an outer cylinder of radius $r_b = 81$ mm. On the outer cylinder, a filled elliptic region centered at $r_0 = 81$ mm, $z_0 = 12$ mm, with “major axis” $\delta z = 14$ mm, and “minor axis” $\delta r = 3$ mm is added. Between the central and the outer metallic parts, a bias $\Delta\phi$ is applied which, combined with the externally applied magnetic field \vec{B} , induces a strong azimuthal $\vec{E} \times \vec{B}$ drift. Due to the upper elliptic region, the electric equipotential lines combined with the magnetic field lines topology lead to the formation of a potential well, see Fig. 3. In this study, a potential well for electron trapping is defined according to Pagonakis *et al.*¹⁸ It is a region where the electric potential energy has a local maximum U_{max} along a

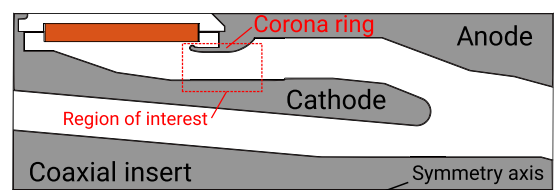


FIG. 2. Cut-view of the electron gun used in the first prototype of the 170 GHz 2 MW coaxial gyrotron designed for ITER. This configuration is used as a model for the geometry considered in this study, see Fig. 1. This representation assumes azimuthal symmetry. Gray indicates a metallic component, orange indicates an insulator, and white represents vacuum.

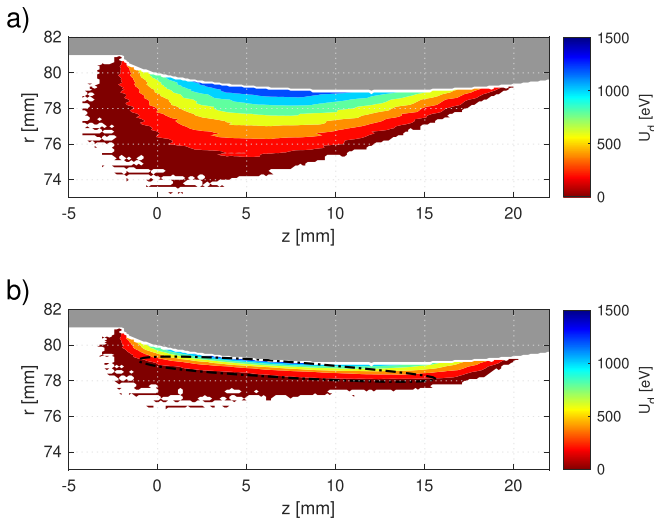


FIG. 3. Potential well position and depth for the geometry of Fig. 1. The plots are zoomed on the well region for readability. In (a), the potential well is represented in the vacuum condition: no electron cloud is present. In (b), the potential well is represented at peak electron density. The black dashed-dotted line represents the cloud edge defined as the positions where $n = 0.2 n_{e,max}$.

magnetic field line. The depth of this potential well is determined by the highest local minimum U_{min} on both sides of U_{max} along the magnetic field line. The maximum depth is $U_d = U_{max} - U_{min}$ as represented in Fig. 4. In the selected case, the well depth spans the range $U_d = 200 - 3600$ eV for a bias $\Delta\phi$ ranging from 5 to 90 kV. We remark that the values of U_d result from a combination of the externally imposed electric field as well as that generated by the space-charge, and so, it can only be known after the simulation is run. In Fig. 3, both the externally imposed well in a vacuum and the self-consistent well in the presence of the cloud are displayed.

Concerning the numerical parameters used to solve the Vlasov–Poisson system, the Finite Element Method (FEM) uses b-splines of degree 2 on a non-uniform grid of 320 subdivisions in z and (45, 70, 35) subdivisions in r where the radial limits for each sub-grid

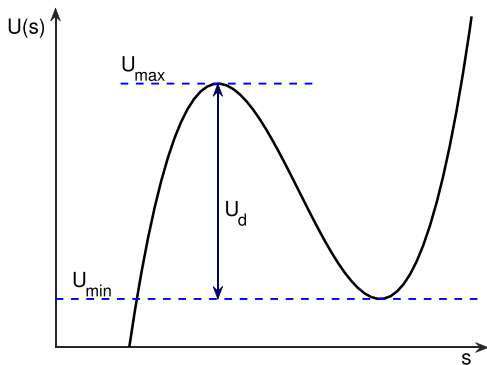


FIG. 4. The potential well depth U_d is defined for a specific magnetic field line as the difference between the local electric potential energy $U(s)$ and the highest local minimum U_{min} along the magnetic field line coordinate s .

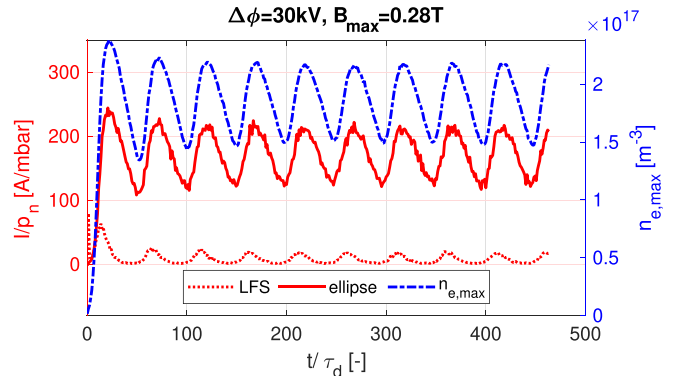


FIG. 5. Time evolution of the peak electron density in the simulation domain (blue) and total axial and radial currents (red). The currents are divided by the RNG pressure in mbar and the time is normalized to the total collision characteristic time scale for the momentum exchange. LFS (Low magnetic Field Side) is the axial current at $z_L = -10$ mm. “Ellipse” is the total radial current collected on the elliptic metallic part. The current on the other boundaries is negligible throughout the simulation.

are (63.75, 72, 79, 81) mm. For the particles, the macro-particle weight is $w_e = 4 \times 10^5$ and the number of macro-particles in the simulations is varying between 1.5 and 2×10^6 . The particle trajectories are then solved using a time step $\Delta t = 2 \times 10^{-12}$ s $\approx 0.016 \times 2\pi/\Omega_{ce}$, where Ω_{ce} is the electron cyclotron frequency. Furthermore, in the simulations, the RNG pressure is artificially increased to allow running for several collision times while resolving cyclotron motion. Indeed, in gyrotrons, due to the low RNG pressure of the order of $p_n = 10^{-8}$ mbar, the collision frequencies are several orders of magnitude smaller than cyclotron or plasma frequencies. As the current code resolves the cyclotron motion, it is necessary to bring these three time scales closer to each other. To this end, the neutral pressure is increased to 10^{-1} mbar. The relatively high pressure sets the collision time scales ($\tau_d \sim 5 \times 10^{-9}$ s) closer to the cyclotronic ($\tau_{ce} \sim 1 \times 10^{-10}$ s at $B \sim 0.28$ T), and plasma time scales ($\tau_{pe} \sim 2.5 \times 10^{-10}$ s at $n \sim 2 \times 10^{17} m^{-3}$), while keeping sufficient time scale separation such that $\tau_d \gg \tau_{ce}$ and $\tau_d \gg \tau_{pe}$. Despite this time scale “compression,” the wall-clock time of a single simulation can be as large as ~ 2 days when running on 36 cpus. As shown later in Sec. III, the results of this study show that simple scaling laws exist for RNG pressure effects that support the choice of high pressures for numerical simulations. This also allows direct extrapolation of the results to arbitrary low neutral pressures. In addition, due to the general availability of total and differential cross section data, and the possibility of future verification against experimental data, the background gas considered in the simulations is Ne. Nevertheless, the simulation results and the reduced model presented in this paper are general and, given the appropriate collision cross sections, can be directly adapted to different kinds of gases such as H₂ or H₂O, typically present in vacuum vessels.⁴⁰

III. RESULTS

A. Time evolution

The simulations are initialized, in the presence of a Ne gas background, with a homogeneous low-density cloud following a Maxwellian distribution with $n_0 = 1 \times 10^{15} m^{-3}$ and an arbitrary low

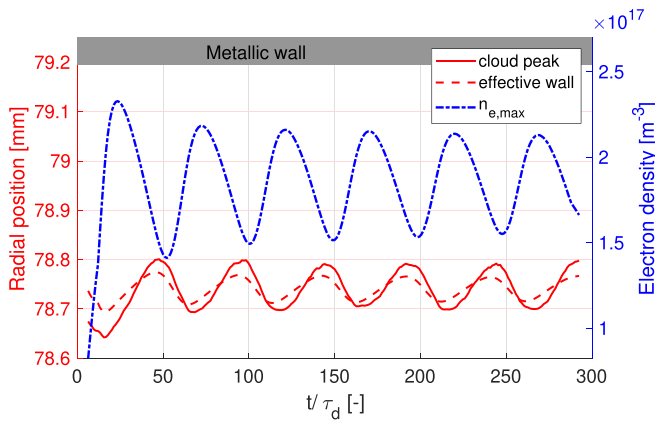


FIG. 6. Time evolution of the instantaneous spatial cloud peak density radial position (solid red) and the effective wall radial position (dashed red) for the simulation shown in Figs. 1 and 5. The effective wall is defined as $r_{\text{wall}}(z_{\text{peak}}) - 2\rho_L(r_{\text{peak}}, z_{\text{peak}}, t)$ with $r_{\text{wall}}(z_{\text{peak}})$ the upper metallic wall radial limit at the axial cloud peak position z_{peak} , and $\rho_L(r_{\text{peak}}, z_{\text{peak}}, t)$ is the instantaneous Larmor radius at the cloud peak position $(r_{\text{peak}}, z_{\text{peak}})$.

temperature $T_0 = 1$ eV. This initial loading accelerates the formation of a trapped electron cloud and reduces the computational time. In addition, the volumetric source is set to a rate of $S = 1.2 \times 10^{21} \text{ m}^{-3} \text{s}^{-1}$ and a temperature $T_s = 1$ eV. The electrons outside of the vacuum potential well, see Fig. 3, are rapidly lost axially. The remaining trapped electrons collide with the RNG, leading to the formation of a cloud. This cloud is located close to the elliptic region where the potential well is deepest, see Fig. 1. The cloud density then slowly increases over time due to ionization and trapping of the newly created electrons. As shown in Fig. 5, as the cloud density increases, a radial current and a comparatively smaller axial current establish, leading to charge losses at the boundaries of the simulation domain. During the cloud formation, the electrons drift radially because of the effective azimuthal drag caused by electron neutral collisions. This drift induces an outward-going radial motion of the cloud peak density, see Fig. 6. At the same time, the density increase causes an increase of the radial electric field amplitude. As the electron perpendicular velocity is strongly dependent on the $\vec{E} \times \vec{B}$ drift, the increase in E_r induces an expansion of the electron Larmor radius ρ_L , which eventually produces particle losses due to gyro-orbits intersecting the wall. It is, thus, useful to define an “effective wall” as a virtual surface distanced by two Larmor radii from the metallic wall. This effective wall defines the radial limit above which electrons can potentially hit the metallic boundary. As shown in Fig. 6, the combination of ρ_L expansion and radial drift of the cloud peak density leads to a moment when the density peak radial position is above the effective wall position. This induces the capture of electrons belonging to the cloud peak density by the metallic wall, causing an important radial loss. As the electron source is directly proportional to the electron density, the system is effectively subjected to a modulated source and a modulated sink and gives rise to oscillations in the cloud density. This effect can be observed in Fig. 5, where both the maximum cloud density and the boundary currents reach a peak after a few tens of τ_d , when the losses start to dominate and oscillations in the peak density and radial current develop. In the absence of a steady electron seed source, the cloud

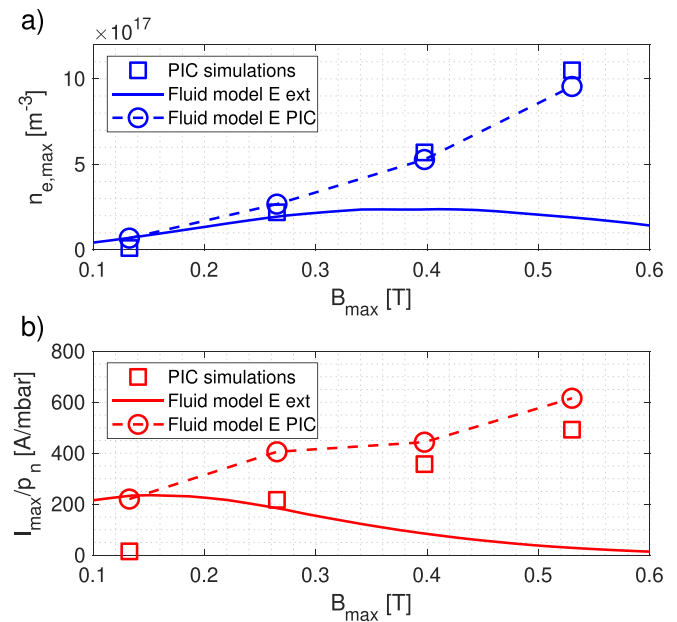


FIG. 7. (a) Evolution of the maximum electron density in the cloud as a function of the maximum magnitude of the magnetic field in the cloud region. (b) Evolution of the maximum radial current, scaled by the RNG pressure, as a function of the maximum magnitude of the magnetic field in the cloud region. The applied bias is $\Delta\phi = 30$ kV, and the RNG pressure is $p_n = 1 \times 10^{-1}$ mbar. For both figures, the squares represent numerical results extracted from the PIC simulations. The dashed-dotted line is a prediction using the model of Sec. IV but using only the external electric field for calculating the collision cross sections, while the circle dotted line is obtained using the full electric field (external plus self-consistent) extracted from the PIC simulations.

is completely lost radially after several tens of τ_d . However, the presence of a steady electron seed source can restart the cloud formation process and the cloud density oscillates between a minimum and a maximum value, in a periodic manner, in what could be called “cloud breathing,” see Fig. 5. It can also be observed from Fig. 5 that the losses are dominantly radial, while axial confinement remains almost ideal.

B. Parametric scans

To understand what are the operational parameters determining the peak density and current amplitudes, parametric scans are performed. The scanned parameters are the maximum magnetic field amplitude $B_{\text{max}} = 0.14 - 0.56$ T, the applied external bias $\Delta\phi = 5 - 90$ kV, and the RNG density $p_n = 10^{-2} - 10^{-1}$ mbar. The results are shown, respectively, in Figs. 7–9. We find that the peak density has a quadratic dependence on the magnetic field amplitude, see Fig. 7(a); it has a non-trivial dependence on the external bias, see Fig. 8(a); and it is independent of the RNG pressure, see Fig. 9(a). Based on the PIC simulation results, the radial current appears to scale linearly with B_{max} , see Fig. 7(b), to have a non-trivial dependency on the external bias, see Fig. 8(b), and, finally, to be linearly proportional to the RNG pressure, see Fig. 9(b). The external bias scan (Fig. 8) suggests the existence of two regimes in the electron peak density and peak current depending on the externally applied bias. Above a certain bias,

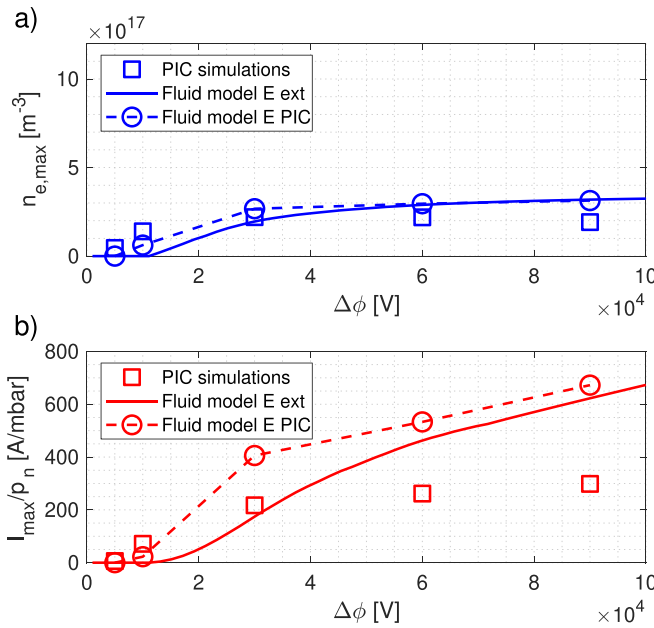


FIG. 8. Same as Fig. 7 but as a function of the electric bias. The magnetic field amplitude is set at $B_{\max} = 0.28$ T, and the RNG pressure is $p_n = 1 \times 10^{-1}$ mbar.

$\Delta\phi > 30$ kV, the slope of the curves changes drastically. An explanation is proposed for these dependencies in Sec. IV.

C. Prevalent force terms

To derive an analytical model that explains the parametric dependencies observed in the simulations, we evaluate the amplitude

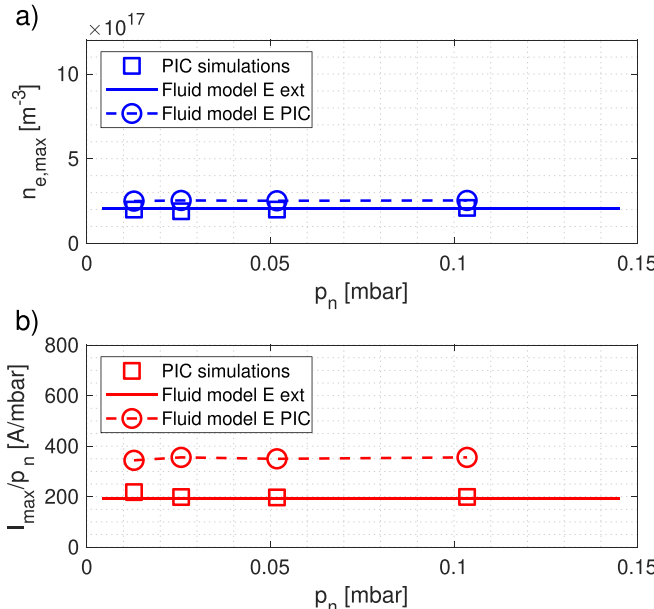


FIG. 9. Same as Fig. 7 but as a function of the RNG pressure. The externally applied bias is set at $\Delta\phi = 30$ kV, and the magnetic field amplitude is set at $B_{\max} = 0.28$ T.

of the different forces acting on the electron fluid, using simulation results. These forces are evaluated by calculating the moments of the distribution function as extracted from the PIC simulations, at a time when the electron density is maximum, and are then averaged over several electron cyclotron periods to reduce numerical noise. The terms considered in the fluid model are the electric and magnetic forces $\vec{F}_E = qn\vec{E}$ and $\vec{F}_B = qn\vec{u} \times \vec{B}$; the inertial term $\vec{F}_i = -mn(\vec{u} \cdot \nabla)\vec{u}$; the pressure term $\vec{F}_p = -\nabla\vec{P}$; the fluid acceleration term $\vec{F}_a = mn\partial_t\vec{u}$; the total collisional drag force term modeled as $\vec{F}_d = -nmn_n\langle\sigma_d v\rangle_f \vec{u}$ which takes into account the effect of elastic collisions, the effect of ionization collisions on the ionizing electrons, and the effective ionization drag due to the production of new low energy electrons by ionization. Here, m and q are the electron mass and charge; n is the fluid density; \vec{E} is the total electric field taking into account external and self-generated components; \vec{u} is the fluid velocity; \vec{B} is the external magnetic field; \vec{P} is the pressure tensor; $\langle \rangle_f$ denotes the average over the electron velocity distribution function; v is the magnitude of the electron velocity, i.e., the electron speed; σ_d is the total electron-neutral collision cross section for momentum exchange; and n_n is the RNG density. In the radial and axial direction, as represented in Figs. 10 and 11, respectively, it can be observed that the dominant terms are the electric and magnetic forces and that the pressure term is one order of magnitude smaller. In these directions, the inertial force term and collisional drag term are completely negligible. In the azimuthal direction, represented in Fig. 12, the dominant terms are the inertial term, the magnetic force, and the collisional drag. In this direction, the pressure force is also smaller than all the other terms. It is also relevant to observe that the sum of all the force terms in each direction is of the order of the numerical noise ($\sum(\vec{F})/\vec{F}_B \ll 1$), providing a verification of the implementation of the numerical model and the reduced fluid model used to describe the effective drag force.

IV. ANALYTICAL MODEL

In this section, an explanation for the parametric dependencies obtained from the simulations, see Figs. 7–9, is proposed.

A. Fluid-Poisson model

A prediction for the cloud average density and the average radial current density can be derived by considering the electron fluid equations coupled to Poisson's equation and neglecting electron pressure effects, which is a simplification that is quantitatively justified by our PIC simulations. We start from the fluid force balance equation

$$mn\left(\frac{\partial\vec{u}}{\partial t} + (\vec{u} \cdot \nabla)\vec{u}\right) = nq(\vec{E} + \vec{u} \times \vec{B}) + \vec{F}_d. \quad (1)$$

As shown in Fig. 10, the dominant radial forces in the bulk of the cloud are the electric and magnetic forces, thus the radial component of Eq. (1) gives

$$u_\theta = -\frac{E_r}{B_z}. \quad (2)$$

As can be seen in Fig. 12, the dominant forces in the azimuthal direction are the inertial force ($\vec{u} \cdot \nabla\vec{u}$ term), the magnetic force, and the drag force. Since $B_r \ll B_z$ and in the cloud we also have $u_z \ll u_r$, we

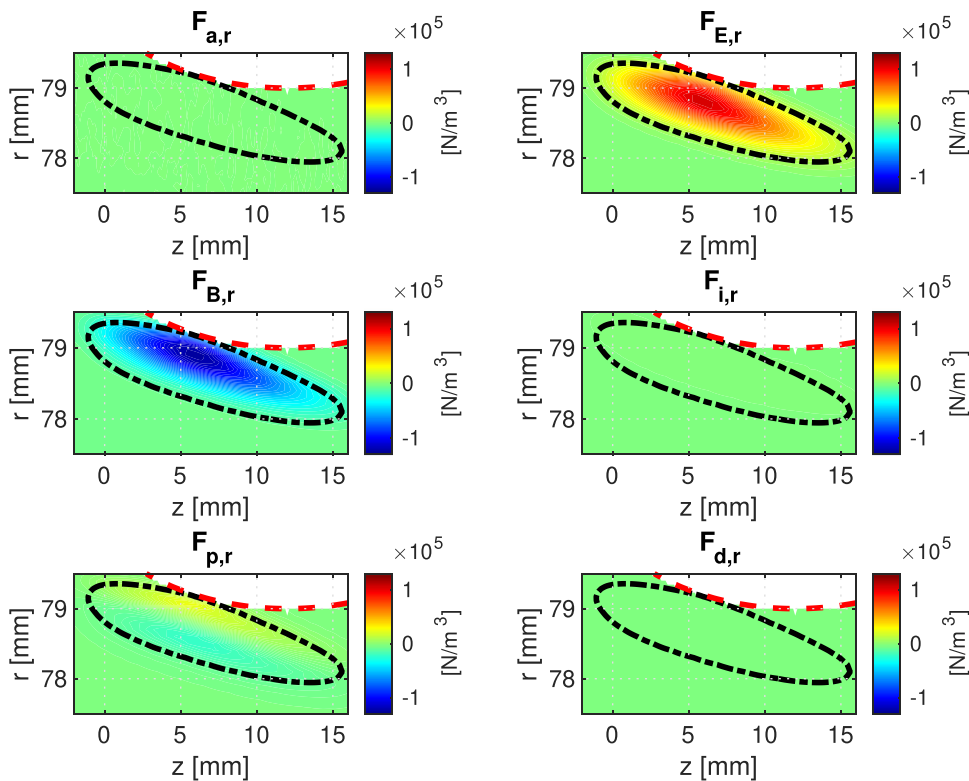


FIG. 10. Contour plot of the different force terms in the radial fluid force balance equation at a time when the number of trapped particles is maximum. The black dashed-dotted line represents the cloud edge defined as the positions where $n = 0.2 n_{e,\max}$. The red dashed line shows the metallic boundary. Here, the subscript r denotes the projection along the radial direction.

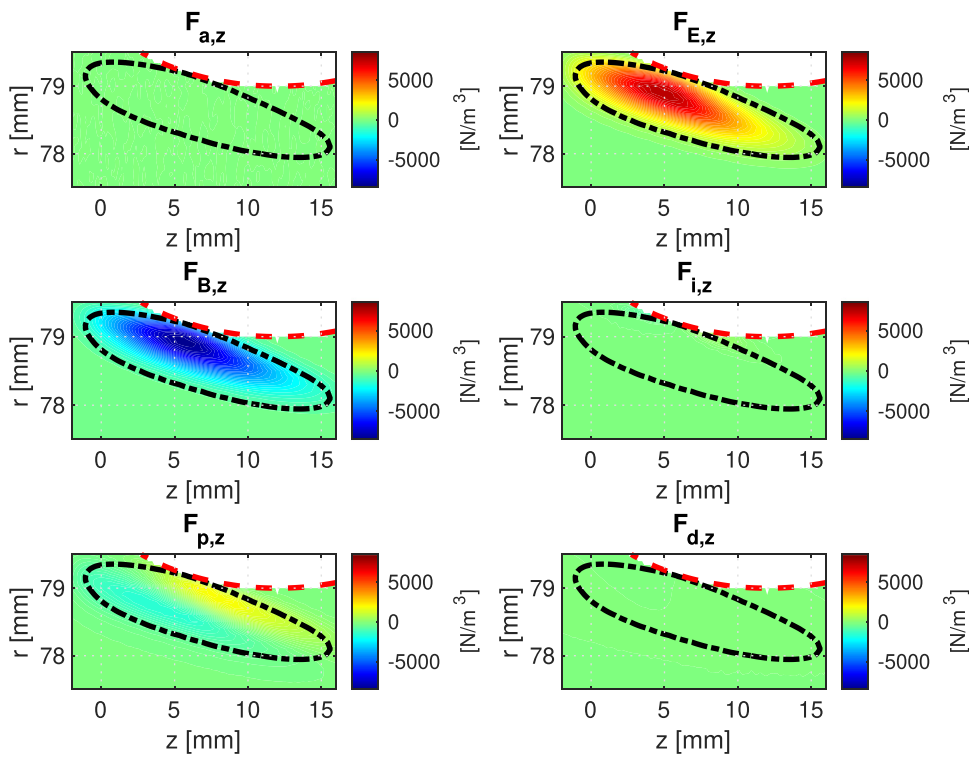


FIG. 11. Same as Fig. 10 for the axial direction. Here, the subscript z denotes the projection along the axial direction.

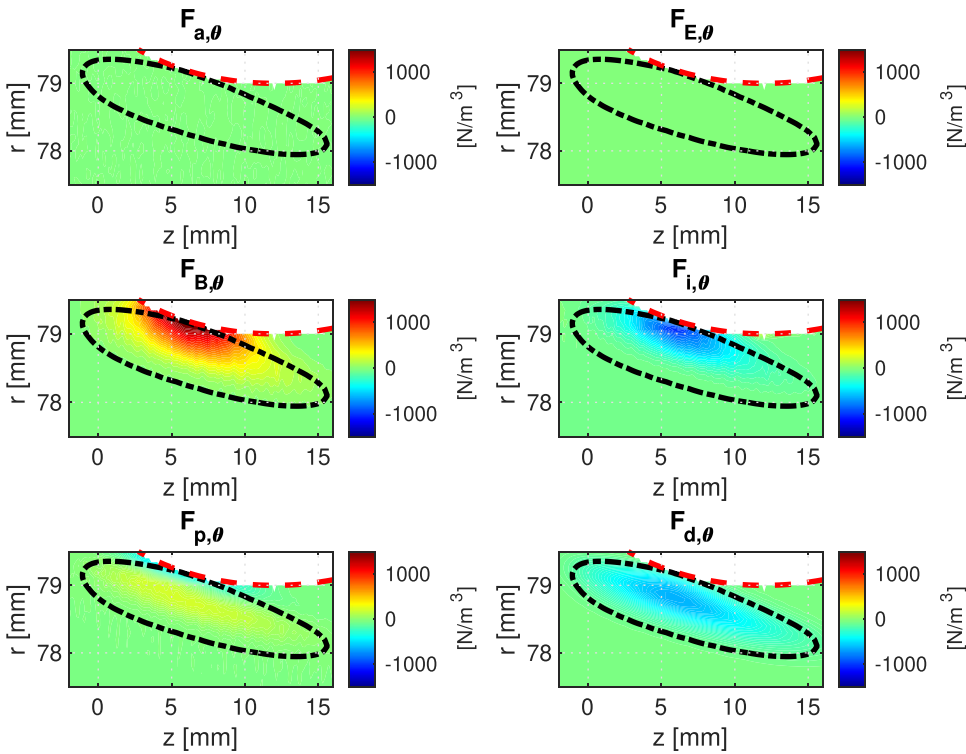


FIG. 12. Same as Fig. 10 for the azimuthal direction. Here, the subscript θ denotes the projection along the azimuthal direction.

can assume $u_z B_r \ll u_r B_z$ and, hence, the azimuthal component of Eq. (1) gives, at equilibrium

$$m u_r \frac{1}{r} \frac{\partial}{\partial r} (r u_\theta) = -q u_r B_z - m n_n \langle \sigma_d v \rangle_f u_\theta. \quad (3)$$

The left-hand side of Eq. (3) can be rewritten by using the expression for the azimuthal velocity, Eq. (2), using Gauss's law, and assuming $|\partial_z E_z| \ll |\frac{1}{r} \partial_r (r E_r)|$ and $\frac{1}{r} \partial_r (r/B_z) \ll \frac{1}{r} \partial_r (r E_r)$. We obtain

$$m u_r \frac{1}{r} \frac{\partial}{\partial r} (r u_\theta) = -m \frac{u_r}{B_z} \frac{1}{r} \frac{\partial}{\partial r} r E_r = -m \frac{u_r q n}{B_z \epsilon_0}. \quad (4)$$

Rewriting Eq. (3) then gives the radial fluid velocity as

$$u_r = -\frac{q n_n \langle \sigma_d v \rangle_f}{m} \frac{E_r}{\omega_p^2 - \Omega_c^2}. \quad (5)$$

Here, $\Omega_c = qB/m$ is the cyclotron frequency and $\omega_p = \sqrt{q^2 n / (\epsilon_0 m)}$ is the plasma frequency.

The time-averaged density can be obtained by starting from the time average of the continuity equation

$$\left\langle \frac{\partial n}{\partial t} + \nabla \cdot (n \vec{u}) \right\rangle_T = \langle n n_n \langle \sigma_{io} v \rangle_f \rangle_T, \quad (6)$$

where σ_{io} is the ionization cross section and $\langle \cdot \rangle_T$ denotes the time average over one cloud breathing oscillation. Considering the case of density oscillations at the spatial peak density

$$\left\langle \frac{\partial t}{\partial t} \right\rangle_T = 0 \quad \text{and} \quad \nabla n = 0; \quad (7)$$

assuming dominant radial losses, azimuthal symmetry and using the radial velocity obtained in Eq. (5), the continuity equation can be rewritten as

$$-\frac{q}{m} \left\langle \frac{n}{r} \frac{\partial}{\partial r} r \left[\frac{n_n \langle \sigma_d v \rangle_f}{\omega_p^2 - \Omega_c^2} E_r \right] \right\rangle_T = \langle n n_n \langle \sigma_{io} v \rangle_f \rangle_T. \quad (8)$$

Using Gauss's law and the fact that $\nabla n = 0$ at the peak density once more as well as the assumptions used in Eq. (4), we obtain an expression for the time-averaged plasma frequency at the spatial peak

$$\omega_{p,\max}^2 = \Omega_c^2 \left\langle \frac{\langle \sigma_{io} v \rangle_f}{\langle \sigma_{io} v \rangle_f + \langle \sigma_d v \rangle_f} \right\rangle_T, \quad (9)$$

which gives directly the average cloud density at the spatial peak $n_{e,\max}$.

Using the radial velocity and average density previously derived, and assuming zero axial velocity, we can also obtain an estimate for the peak current by integrating the loss term $\nabla \cdot (n \vec{u})$ over the cloud volume

$$I = \int \langle q \nabla \cdot (n \vec{u}) \rangle_T dV \approx -2\pi L r_+ \epsilon_0 n_{e,\max} \langle E_r \langle \sigma_{io} v \rangle_f \rangle_T, \quad (10)$$

where L is the characteristic cloud axial length and r_+ is the cloud outer radial limit. These geometric quantities can be estimated from the potential well dimensions in a vacuum. It can be observed that this current is linearly proportional to the RNG density but has a more complex scaling in the electric and magnetic field due to the non-trivial dependency of $\langle \sigma_{io} v \rangle$ on these terms.

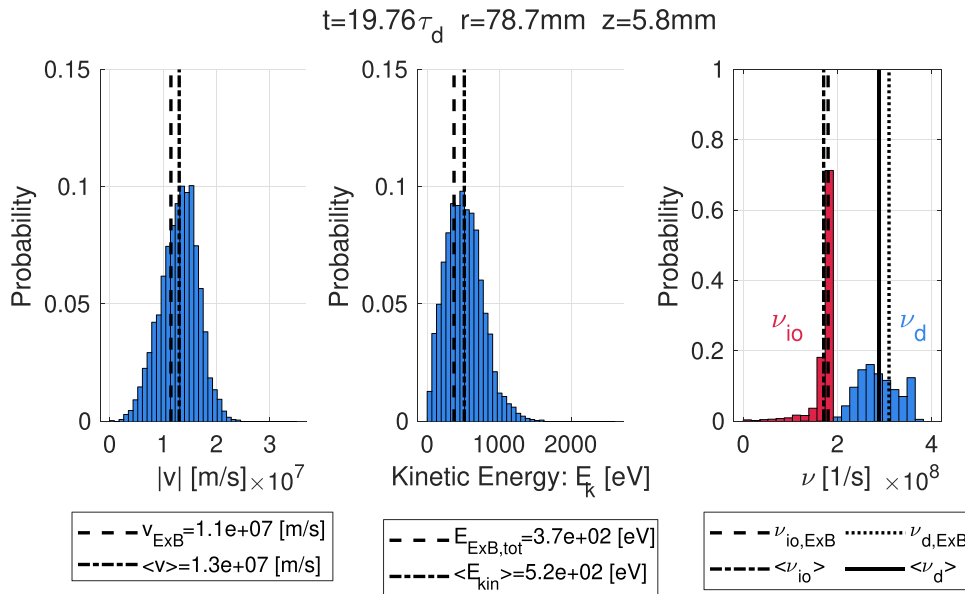


FIG. 13. Electron velocity distribution (left), kinetic energy distribution (middle), and collision frequencies distribution (right) extracted from the PIC simulation shown in Figs. 1 and 5 and represented at a time when the density is maximum and at the position of peak density. For comparison, the average is represented by the dash-dotted and solid lines. The dashed lines and the dotted line are the equivalent quantity if the velocity of the electron is exactly the local $\vec{E} \times \vec{B}$ velocity.

B. Model verification

To predict the peak electron density and current using Eqs. (9) and (10), it is necessary to calculate the collision frequencies by averaging $\sigma\nu$ over the electron velocity distribution function. As can be observed in Fig. 13, due to the large $\vec{E} \times \vec{B}$ drift, the average speed of electrons is dominated by the azimuthal component of the average velocity such that $\vec{u} \approx \vec{E} \times \vec{B}/B^2$. Furthermore, the variance of the speed distribution and the variance of the kinetic energy distribution are relatively small. We may, therefore, approximate the collision frequencies ν as follows:

$$\nu = n_n \langle v \sigma(E_k) \rangle_f \approx n_n \left| \frac{\vec{E} \times \vec{B}}{B^2} \right| \sigma \left(\frac{1}{2} m \frac{|\vec{E} \times \vec{B}|^2}{B^4} \right). \quad (11)$$

Here, $E_k = mv^2/2$ is the kinetic energy of the electrons. The quality of this approximation can be assessed by looking at the figure on the right-hand side of Fig. 13, where we see a close agreement between the collision frequencies directly computed from the PIC simulations, and the approximate collision frequencies given by Eq. (11). With these definitions, Eqs. (9) and (10) are used to verify the analytic model for the parametric scans of Sec. III. To calculate the collision frequencies, the drift velocity is calculated once using only the externally imposed electric field (dashed line in Figs. 7–9) and once using the total electric field extracted from the simulations (circles in Figs. 7–9). The comparison between the simulation results and the model predictions shows that the knowledge of the total electric field is necessary to obtain the correct scaling. When using the total electric field in the model, Eqs. (9) and (10), the analytical scalings for the scans on B_{\max} , see Fig. 7, on $\Delta\phi$, see Fig. 8, and on p_n , see Fig. 9, are well reproduced for $n_{e,\max}$, and the trends are captured for I_{\max} . The slightly worse agreement for the current could be explained by the approximated size of the cloud which is assumed independent of the external parameters. These results reveal that a model for the self-consistent electric

field is needed to have an analytical prediction from the reduced model and limit the need for computationally expensive numerical simulations.

It appears from this reduced model that a fluid code could be sufficient to study the problem at hand. However, this model considers only the time-averaged behavior of the cloud, and it is not yet known if kinetic effects are important to describe the dynamics (cloud breathing). Moreover, in a fluid code, the implementation of boundary conditions for the fluid would be much more complicated. Furthermore, as seen in Fig. 12, the amplitude of the pressure force in the azimuthal direction, while small, is not completely negligible. This means that, if this term is important to describe the dynamics of the system, the use of an isothermal fluid model is not justified for a two-dimensional fluid model, and a more complex closure equation is necessary.

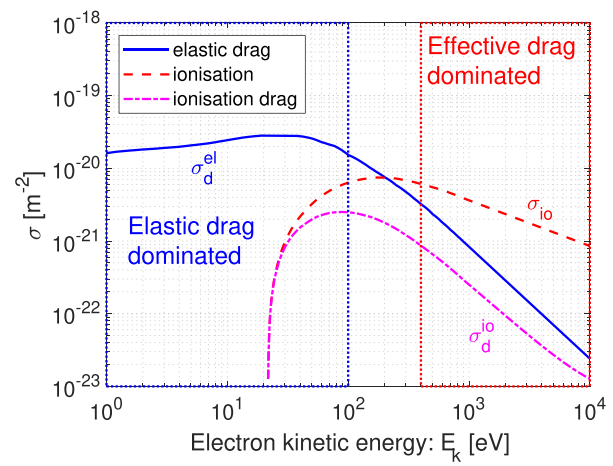


FIG. 14. Electron collision cross sections of Ne atoms as a function of the electron kinetic energy. The neutral particles are assumed to have zero velocity.

C. Collision regimes

In the parametric scans on the external bias of Fig. 8, two regimes have been identified for both the current and the peak electron density, where a plateau is reached at large biases (above $\Delta\phi = 30$ kV). This result can be explained by examining the collision cross sections, represented in Fig. 14, and their corresponding effective drag frequencies. Here, two main regimes can be defined. For low electron kinetic energies, $E_k \leq 100$ eV, the elastic drag dominates and the peak densities depend directly on the electron energies and by extension on the externally applied electric and magnetic fields, see Eqs. (11) and (9). On the contrary, for high-electron kinetic energies, $E_k \gtrsim 400$ eV, the effective drag due to electron creation dominates. This means that, in Eq. (9), $\sigma_d = \sigma_{io} + \sigma_d^{el} + \sigma_d^{io} \approx \sigma_{io}$ and the peak electron density become independent of the electron energies

$$\omega_{pe,peak}^2 = \left\langle \Omega_{ce}^2 \frac{\langle \sigma_{io} v \rangle_f}{\langle \sigma_{io} v \rangle_f + \langle \sigma_d v \rangle_f} \right\rangle_T \approx \frac{1}{2} \Omega_{ce}^2. \quad (12)$$

In the PIC simulations, this change of regime is expected for biases $\Delta\phi \approx 30$ kV, where the electron kinetic energy is $E_k \approx 200$ eV. Furthermore, as the current is linearly proportional to the cloud density, two regimes are also expected in the dependence on the external bias for this quantity.

V. DISCUSSION AND OUTLOOK

A new PIC code has been developed that is able to simulate the self-consistent formation of an electron cloud in a configuration close to the one existing in gyrotron electron guns. It is shown that electron clouds form inside the potential well (which results from a combination of the external magnetic field and of the self-consistent electric field) and that such clouds are the source of important radial currents. Parametric scans are presented that show the dependency of the peak electron cloud density and radial current on external parameters. To explain the observed dependencies, an analytical fluid-Poisson model is derived and successfully validated with the simulation results using the PIC code. This model shows that the radial current is linearly dependent on the RNG pressure, which permits the artificial increase of the collision frequencies, and is important for the applicability of the code and its relevance in the design process of gyrotron guns (to provide shorter calculation times). This model also confirms the quadratic dependence of the peak density on the magnetic field amplitude. Finally, this article reveals and explains that, depending on the trapped electrons kinetic energies, two collision regimes can be identified. In the first regime, the radial transport is dominated by elastic collision drag and the electron cloud density is proportional to the electric and magnetic field amplitude. In contrast, in the second regime, the transport is dominated by the effective drag imposed by the release of electrons from ionization, and the electron density is only proportional to the magnetic field amplitude. It is, however, important to stress that this model does not capture the dynamics of the system and cannot explain the oscillations in the radial current and peak density. The development of an extended model relaxing the equilibrium assumption is planned and could encompass pressure effects, density gradient effects, or non-uniform energy distributions effects currently neglected in the reduced model. Furthermore, the radial currents, when scaled using a realistic pressure of $p_n = 1 \times 10^{-8}$ mbar, are of the order of $I \approx 1 \mu\text{A}$ which is too low compared to previous experiments and

would not cause detrimental effects. These discrepancies can potentially be explained by a rapid loss of particles due to diocotron instabilities, which may lead to current pulses, or by an oversimplification of the geometry and of the resulting potential well. To verify these hypotheses, one solution would be to break the azimuthal symmetry, which is, however, numerically expensive. Another solution would be to use models based on diocotron linear stability equations with density profiles extracted from the current PIC code. To study geometric effects, the current Poisson solver is currently being adapted to allow for more realistic geometries. In parallel to this study, and to the numerical research, a new experiment is currently being developed at the Swiss Plasma Center. Such experiment will reproduce the key characteristics of the gyrotron electron gun, in particular, in terms of geometries, applied fields amplitudes and topologies, and pressure. The aim is to study such electron clouds. This will broaden the view on the current subject and provide input to address the weak points of the presented model. The experiment will further guide the theoretical research and help validating the current PIC code and reduced models.

ACKNOWLEDGMENTS

A. Cerfon wishes to thank Paolo Ricci and the Swiss Plasma Center at EPFL for hosting him during the academic year 2020–2021, during which some of the research work presented here was performed. The authors also wish to thank Trach Minh Tran, Patryk Kaminski, and Jérémie Genoud, for the development of FEM libraries and the initial version of the PIC code on which the current code is built.

This work has been carried out within the framework of the EUROfusion Consortium, funded by the European Union via the Euratom Research and Training Programme (Grant Agreement No 101052200–EUROfusion). Views and opinions expressed are, however, those of the author(s) only and do not necessarily reflect those of the European Union or the European Commission. Neither the European Union nor the European Commission can be held responsible for them.

The calculations have been performed using the facilities of the Scientific IT and Application Support Center of EPFL.

This work was supported, in part, by the Swiss National Science Foundation under Grant No. 204631.

AUTHOR DECLARATIONS

Conflict of Interest

The authors have no conflicts to disclose.

Author Contributions

Guillaume Le Bars: Conceptualization (equal), Data curation (lead), Formal analysis (lead), Investigation (equal), Methodology (equal), Software (lead), Validation (lead), Visualization (lead), Writing – original draft (lead), and Writing – review and editing (equal). **Jean-Philippe Hogge:** Conceptualization (lead), Formal analysis (equal), Funding acquisition (equal), Methodology (equal), Project administration (lead), Supervision (equal), Visualization (supporting), and Writing – review and editing (supporting). **Joaquim Loizu:** Conceptualization (equal), Formal analysis (equal), Funding acquisition (equal), Methodology (equal), Project administration (lead),

Supervision (equal), Visualization (supporting), and Writing – review and editing (lead). **Stefano Alberti:** Conceptualization (equal), Formal analysis (equal), Funding acquisition (equal), Methodology (equal), Supervision (equal), Visualization (supporting), and Writing – review and editing (equal). **Francesco Romano:** Investigation (equal), Supervision (supporting), Visualization (supporting), and Writing – review and editing (equal). **Antoine Julien Cerfon:** Methodology (supporting), Software (supporting), Validation (supporting), and Writing – review and editing (equal).

DATA AVAILABILITY

The data that support the findings of this study are available from the corresponding author upon reasonable request.

REFERENCES

- ¹M. Vogel, *Particle Confinement in Penning Traps*, Springer Series on Atomic, Optical, and Plasma Physics Vol. 100 (Springer International Publishing, Cham, 2018).
- ²R. C. Davidson, *Physics of Nonneutral Plasmas* (World Scientific Publishing Co., 2001).
- ³K. R. Chu, “The electron cyclotron maser,” *Rev. Mod. Phys.* **76**, 489–540 (2004).
- ⁴D. H. E. Dubin and T. M. O’Neil, “Trapped nonneutral plasmas, liquids, and crystals (the thermal equilibrium states),” *Rev. Mod. Phys.* **71**, 87–172 (1999).
- ⁵J. H. Malmberg and C. F. Driscoll, “Long-time containment of a pure electron plasma,” *Phys. Rev. Lett.* **44**, 654–657 (1980).
- ⁶Y. H. Jo, J. S. Kim, G. Stancari, M. Chung, and H. J. Lee, “Control of the diocotron instability of a hollow electron beam with periodic dipole magnets,” *Phys. Plasmas* **25**(1), 011607 (2018).
- ⁷V. V. Mikhailyenko, J. Seok Kim, Y. Jo, V. S. Mikhailyenko, and H. June Lee, “Non-modal analysis of the diocotron instability for cylindrical geometry with conducting boundary,” *Phys. Plasmas* **21**(5), 052105 (2014).
- ⁸I. N. Kartashov and M. V. Kuzlev, “Nonlinear dynamics of diocotron instability,” *Plasma Phys. Rep.* **36**, 524–532 (2010).
- ⁹J. Pétri, “Non-linear evolution of the diocotron instability in a pulsar electro-sphere: Two-dimensional particle-in-cell simulations,” *Astron. Astrophys.* **503**(1), 1–12 (2009).
- ¹⁰I. A. Kotelnikov, R. Pozzoli, and M. Romé, “Diocotron instability in non-neutral plasmas with a stationary point in the rotation frequency profile,” *Phys. Plasmas* **12**(9), 092105 (2005).
- ¹¹T. J. Hilsabek, “Finite length and trapped-particle diocotron modes,” Ph.D. thesis (UCLA, 2003).
- ¹²A. A. Kabantsev and C. F. Driscoll, “End shape effects on the $m_0 = 1$ diocotron instability in hollow electron columns,” *AIP Conf. Proc.* **498**(1), 208–213 (1999).
- ¹³R. Schultd and E. Borie, “Diocotron instability of the electron beam in the drift tube of a gyrotron,” *Int. J. Infrared Millimeter Waves* **16**(10), 1675–1700 (1995).
- ¹⁴C. F. Driscoll, “Observation of an unstable $l = 1$ diocotron mode on a hollow electron column,” *Phys. Rev. Lett.* **64**, 645–648 (1990).
- ¹⁵L. F. Ricketson and A. J. Cerfon, “Sparse grid techniques for particle-in-cell schemes,” *Plasma Phys. Controlled Fusion* **59**(2), 024002 (2016).
- ¹⁶S. Muralikrishnan, A. J. Cerfon, M. Frey, L. F. Ricketson, and A. Adelmann, “Sparse grid-based adaptive noise reduction strategy for particle-in-cell schemes,” *J. Comput. Phys. X* **11**, 100094 (2021).
- ¹⁷I. G. Pagonakis, J. Hogge, T. Goodman, S. Alberti, B. Piosczyk, S. Illy, T. Rzesnicki, S. Kern, and C. Lievin, “Gun design criteria for the refurbishment of the first prototype of the EU 170 GHz/2 MW/CW coaxial cavity gyrotron for ITER,” in *2009 34th International Conference on Infrared, Millimeter, and Terahertz Waves* (IEEE, 2009), pp. 1–2.
- ¹⁸I. G. Pagonakis, B. Piosczyk, J. Zhang, S. Illy, T. Rzesnicki, J.-P. Hogge, K. Avramidis, G. Gantenbein, M. Thumm, and J. Jelonnek, “Electron trapping mechanisms in magnetron injection guns,” *Phys. Plasmas* **23**, 023105 (2016).
- ¹⁹S. Alberti, “Magnetic confinement fusion: Plasma heating with millimetre waves,” *Nat. Phys.* **3**, 376–377 (2007).
- ²⁰C. Darbos, F. Albajar, T. Bonicelli, G. Carannante, M. Cavinato, F. Cismondi, G. Denisov, D. Farina, M. Gagliardi, F. Gandini, T. Gassmann, T. Goodman, G. Hanson, M. A. Henderson, K. Kajiwara, K. McElhaney, R. Nousiainen, Y. Oda, T. Omori, A. Oustinov, D. Parmar, V. L. Popov, D. Purohit, S. L. Rao, D. Rasmussen, V. Rathod, D. M. S. Ronden, G. Saibene, K. Sakamoto, F. Sartori, T. Scherer, N. P. Singh, D. Strauß, and K. Takahashi, “Status of the ITER electron cyclotron heating and current drive system,” *J. Infrared, Millimeter, Terahertz Waves* **37**(1), 4–20 (2016).
- ²¹R. Ambrosino, “DTT-divertor tokamak test facility: A testbed for DEMO,” *Fusion Eng. Des.* **167**, 112330 (2021).
- ²²S. Garavaglia, G. Aiello, S. Alberti, K. Avramidis, A. Bruschi, I. G. Chelis, J. Franck, G. Gantenbein, G. Granucci, G. Grossetti, K. Hizanidis, S. Illy, J. Jelonnek, P. Kalaria, G. Latsas, A. Moro, I. Pagonakis, D. V. Peponis, E. Poli, N. Rispoli, S. Ruess, T. Rzesnicki, T. Scherer, D. Strauss, M. Thumm, I. Tigelis, C. Tsironis, C. Wu, T. Franke, and M. Q. Tran, “EU DEMO EC system preliminary conceptual design,” in *Proceedings of the 13th International Symposium on Fusion Nuclear Technology (ISFNT-13)*, 2018 [Fusion Eng. Des.] **136**, 1173–1177 (2018).
- ²³H. P. Laqua, J. Baldzuhn, H. Braune, S. Bozhenkov, K. J. Brunner, Y. O. Kazakov, S. Marsen, D. Moseev, T. Stange, R. C. Wolf, and M. Zanini, “Overview of W7-X ECRH results,” *EPJ Web Conf.* **203**, 02002 (2019).
- ²⁴M. H. Douglas and T. M. O’Neil, “Transport of a nonneutral electron plasma due to electron collisions with neutral atoms,” *Phys. Fluids* **21**, 920–925 (1978).
- ²⁵R. C. Davidson and E. H. Chao, “Nonlinear expansion and heating of a non-neutral electron plasma due to elastic collisions with background neutral gas,” *Phys. Plasmas* **3**, 2615–2619 (1996).
- ²⁶R. C. Davidson and D. A. Moore, “Expansion and nonlinear relaxation of a strongly magnetized non-neutral electron plasma due to elastic collisions with background neutral gas,” *Phys. Plasmas* **3**, 218–225 (1996).
- ²⁷J. I. Javakhishvili, G. N. Kervalishvili, and N. A. Kervalishvili, “Nonlinear evolution of a nonneutral electron gas-discharge plasma with nonzero electron temperature,” *Phys. Lett. A* **258**, 349–353 (1999).
- ²⁸N. A. Kervalishvili, “Collisional nonlinear evolution of a cold nonneutral electron plasma,” *Phys. Lett. A* **270**, 186–190 (2000).
- ²⁹K. Höllig, *Finite Element Methods With B-Splines: Frontiers in Applied Mathematics* (Society for Industrial and Applied Mathematics, 2003).
- ³⁰K. Höllig, U. Reif, and J. Wipper, “Weighted extended B-spline approximation of Dirichlet problems,” *SIAM J. Numer. Anal.* **39**, 442–462 (2001).
- ³¹C. K. Birdsall and A. B. Langdon, *Plasma Physics via Computer Simulation* (CRC Press, Boca Raton, 2017).
- ³²C. Birdsall, “Particle-in-cell charged-particle simulations, plus Monte Carlo collisions with neutral atoms, PIC-MCC,” *IEEE Trans. Plasma Sci.* **19**, 65–85 (1991).
- ³³M. Sengupta and R. Ganesh, “Influence of electron-neutral elastic collisions on the instability of an ion-contaminated cylindrical electron cloud: 2D3V PIC-with-MCC simulations,” *Phys. Plasmas* **23**, 102111 (2016).
- ³⁴See www.lxcat.net for “Biagi-v8.9 Database, Private Communication” (last accessed June 1, 2021).
- ³⁵S. F. Biagi, see lxcat.net for “Fortran Program, Magboltz v8.9” (2021).
- ³⁶J. Fajans, “Transient ion resonance instability,” *Phys. Fluids B* **5**, 3127–3135 (1993).
- ³⁷A. Ohkrimovskyy, A. Bogaerts, and R. Gijbels, “Electron anisotropic scattering in gases: A formula for Monte Carlo simulations,” *Phys. Rev. E* **65**, 037402 (2002).
- ³⁸C. B. Opal, W. K. Peterson, and E. C. Beaty, “Measurements of secondary-electron spectra produced by electron impact ionization of a number of simple gases,” *J. Chem. Phys.* **55**, 4100–4106 (1971).
- ³⁹I. G. Pagonakis, K. A. Avramidis, G. Gantenbein, T. Rzesnicki, A. Samartsev, and J. Jelonnek, “Magnetic field profile analysis for gyrotron experimental investigation,” *Phys. Plasmas* **24**, 033102 (2017).
- ⁴⁰S. Mukherjee, P. Panchal, J. S. Mishra, R. Gangradey, P. Nayak, and V. Gupta, “Hydrogen outgassing and permeation in stainless steel and its reduction for UHV applications,” *Mater. Today* **44**, 968–974 (2021).